Contents

A Appendix: Uncertainty Analysis

A.1 Uncertainty Analysis Approach of the 2C-PIV Data

The uncertainty analysis follows the footsteps by Lazar *et al.* [8] and Wolf [16]. The error sources introduced hereafter encompass the equipment, the particle response in the fluid and statistical error due to sampling. The first two uncertainties address errors of an instantaneous PIV (particle image velocimetry) result, the latter is the result of the finite sample size.

The individual uncertainties are combined to a total 95% confidence level of the velocity $E_{95,U}$ as given eq. (A.1). Here, $\partial U/\partial P_m$ denotes the sensitivity of the velocity U to a parameter P_m, while $m = 1...M$ encompasses the number of the multiple, statistically independent parameters P_m.

$$E_{95,U} = \sqrt{\sum_{m=1}^{M} \left(\frac{\partial U}{\partial P_m} E_{95,m} \right)^2} \tag{A.1}$$

A.1.1 Confidence Levels of Instantaneous Samples

A.1.1.1 Equipment

The current uncertainty evaluation introduced by the equipment is assessed as exercised in Lazar *et al.* [8] and Wolf [16]. The relation of the velocity is given in eq. (A.2) where Ψ corresponds to the scaling magnification and $\tilde{U}$ to the PIV velocity measurement in a pixel-time reference frame. The latter can be expressed as ratio between the displacement Δs between the image pairs and the delay time Δt between the two laser pulses.

$$U = \Psi(l,L,\lambda) \cdot \tilde{U}(s,t) = \Psi(l,L,\lambda) \cdot \frac{\Delta s}{\Delta t} \tag{A.2}$$

This requires a relation for the scaling magnification Ψ, which is given in eq. (A.3). The parameter l denotes the distance on the calibration scales in length units, while L corresponds to the same distance on the recorded image in pixel units. The scaling magnification can alternatively be expressed as ratio between the distance λ from the calibration scale to the lens and the focal length f.

$$\Psi = \frac{l}{L} = \frac{\lambda}{f} \tag{A.3}$$

The equation for the velocity eq. (A.2) shows that the calibration of the scaling magnification and the timing accuracy is taken into account as most relevant parameters. Thus, it can be expressed as given in eq. (A.4). There, $E_{0.95,i}$ represents a confidence level of 95% of parameter i. If eq. (A.2) and eq. (A.3) is taken into account, this partial differential equation can be expressed as shown in eq. (A.5) and eq. (A.6). The latter equation shows that the equipment-based uncertainty is a function of the local velocity.

$$E_{0.95,U} = \sqrt{\underbrace{\left(\frac{\partial U}{\partial l}E_{0.95,l}\right)^2 + \left(\frac{\partial U}{\partial L}E_{0.95,L1}\right)^2 + \left(\frac{\partial U}{\partial L}E_{0.95,L2}\right)^2 + \left(\frac{\partial U}{\partial \lambda}E_{0.95,\lambda}\right)^2 \ldots}_{\text{scaling magnification}} + \underbrace{\left(\frac{\partial U}{\partial t1}E_{0.95,t1}\right)^2 + \left(\frac{\partial U}{\partial t2}E_{0.95,t2}\right)^2}_{\text{timing accuracy}}} \tag{A.4}$$

$$E_{0.95,U} = \sqrt{\tilde{U}^2\left[\left(\frac{1}{L}E_{0.95,l}\right)^2 + \left(\frac{-l}{L^2}E_{0.95,L1}\right)^2 + \left(\frac{-l}{L^2}E_{0.95,L2}\right)^2 + \left(\frac{l}{\lambda L}E_{0.95,\lambda}\right)^2\right] \ldots + \left(\frac{-\tilde{U}}{\Delta t}\frac{l}{L}\right)^2\left[E_{0.95,\Delta t1}^2 + E_{0.95,\Delta t2}^2\right]} \tag{A.5}$$

$$E_{0.95,U} = U\sqrt{\left[\left(\frac{1}{l}E_{0.95,l}\right)^2 + \left(\frac{1}{L}E_{0.95,L1}\right)^2 + \left(\frac{1}{L}E_{0.95,L2}\right)^2 + \left(\frac{1}{\lambda}E_{0.95,\lambda}\right)^2\right] \ldots + \left(\frac{1}{\Delta t}\right)^2\left[E_{0.95,\Delta t1}^2 + E_{0.95,\Delta t2}^2\right]} \tag{A.6}$$

A.1.1.2 Particle Dynamics

In the following, the ability of the particle to faithfully follow the flow is assessed. In fact, a multitude of forces are acting on a particle in the flow field, but a number of simplifications can be made since the density of the seeding particle in PIV is usually larger by several orders of magnitude than the fluid density. In the frame of the current considerations, it is assumed that the particle dynamics is dependent on the ratio between the drag of the particle and the inertial force [10]. Lazar *et al.* [8] presents an approximation for the velocity lag of a particle with respect to the flow. The corresponding equation is shown in eq. (A.7), which inherently contains the approximation of the drag as suggested by Stokes [13]. The particle lag becomes a linear function of the particle's acceleration.

$$U_F - U_P = \frac{1}{18}\frac{\rho_P d_P^2}{\mu_F}\frac{dU_P}{dt} \qquad \text{with: } \frac{dU_P}{dt} \approx \frac{\partial U_P}{\partial x_P}\underbrace{\frac{dx_P}{dt}}_{\sim u} + \frac{\partial U_P}{\partial y_P}\underbrace{\frac{dy_P}{dt}}_{\sim v} \tag{A.7}$$

A.1.2 Confidence Levels of Mean and Fluctuation Statistics

In the current section, the approach for the statistical uncertainty associated with the sampling of the PIV measurements is presented. In detail, this concerns the *sampling errors* for the mean and the turbulent velocity, which are a result of the finite length of the sample size N. The current approach is extracted from the work by Benedict and Gould [2].

The sampling-related 95% confidence interval $E_{0.95}$ of a series of uncorrelated samples is given by eq. (A.8) where the quantity s_x^2 describes the variance of the estimated mean of a property x. Benedict and Gould [2] provides the estimator variances for the quantities of interest here, which is consequently replaced. For any distribution, the corresponding 95% confidence interval for the mean velocity is represented by eq. (A.9), and for the turbulent intensity $\sqrt{\overline{U'^2}}$, it is given by eq. (A.10).

$$E_{0.95}(\text{sampling}) = \pm 1.96 \cdot \sqrt{\frac{s_x^2}{N}} \tag{A.8}$$

$$s_x^2 = \overline{U'^2} \qquad \text{for } E_{0.95,\overline{U}} \tag{A.9}$$

$$s_x^2 = \frac{\overline{U'^4} - \overline{U'^2}^2}{4\overline{U'^2}} \qquad \text{for } E_{0.95,\sqrt{\overline{U'^2}}} \tag{A.10}$$

A.2 Uncertainty Analysis for the Wake Flow

The methods above are now applied on the wake flow for the determination of the corresponding uncertainty estimation.

A.2.1 Confidence Levels of Instantaneous Samples

First, the uncertainty of instantaneous samples is determined.

Table A.1: Summary of equipment uncertainty parameters for the Mach 0.8-case (V164) focusing on the wake flow. The abbreviation n.a. stands for not available.

Category	Parameter	Description	y_i	$E_{0.95,i}$
Calibration	l	Calibration scale physical length	133.9 mm	10 μm
	L1	Calibration scale image plane length	1600 px	1px
	L2	Image distortion due to aberrations	1600 px	3.8 px
	λ	Distance from calibration scale to lens	395 mm	0.5 mm
Timing	$\Delta t1$	Laser pulse timing	n.a.	n.a.
	$\Delta t2$	Accuracy of timing unit	n.a.	n.a.
	Δt	Combined t1 and t2	2.6 μs	2.6 ns

A.2.1.1 Equipment

The equipment-related uncertainty is determined according to approach given in section A.2.1.1. The relevant parameters are listed in table A.1 for the wake flow at Mach 0.8 (V164). The uncertainty for the calibration length is approximated, as well as the ones regarding the calibration procedure on the image plane and the distance from the calibration scale to lens. Remember that the latter describes the requirement of aligning the calibration scale exactly along the laser light sheet. The aberration of the lens is extracted from the corresponding technical data sheet of the manufacturer (see section 2, Methods). The timing uncertainty between two laser pulses, or *jitter*, has been determined experimentally for the current system. The PIV system encompasses a timing unit and the laser system itself for which a maximum combined uncertainty of $E_{0.95,\Delta t} = 2.6\,\mathrm{ns}$ was determined between two laser pulses.

According to eq. (A.11), this results in a hardware-induced confidence level of $E_{0.95,U} = 0.29\% \cdot U$ for wake flow. The influence of the various terms is listed in a precursor step and one can see that the contribution of the calibration scale is negligible in comparison to the rest. For the wake flow investigations, the contribution due to the distortion of the lens is largest, while, as shown below, the timing becomes more dominant for the boundary layer considerations. In summary though, the influence of the equipment on the uncertainty of an instantaneous result is small.

$$\begin{aligned} E_{0.95,U} &= U \left(\underbrace{5.6 \cdot 10^{-9}}_{\mathrm{l}} + \underbrace{0.4 \cdot 10^{-6}}_{\mathrm{L1}} + \underbrace{5.6 \cdot 10^{-6}}_{\mathrm{L2}} + \underbrace{1.6 \cdot 10^{-6}}_{\lambda} + \underbrace{1.0 \cdot 10^{-6}}_{\Delta t} \right)^{0.5} \\ &= 0.0029 \cdot U \qquad \text{for the wake flow at Mach } 0.8 \text{ (V164)} \end{aligned} \tag{A.11}$$

As shown in the overview of table A.2, the same order of magnitude for the equipment-based uncertainties can be found for the experiments at the other various Mach numbers. Note that this overview also contains data of further uncertainties presented over the course of the coming sections.

Table A.2: Overview of the upper bound of the 95% confidence interval for the instantaneous samples for the wake flow. It is given in percent of the free-stream velocity. In detail, the table encompasses the equipment-related (*Equip.*), the particle-slip-related (*Slip*), and the total instantaneous (*Total inst.*) uncertainty for the investigated Mach numbers. For the equipment-related bound, the linear factor *fac* as determined by means of eq. (A.6) is additionally provided. The abbreviation *avg* denotes the spatially averaged uncertainty in the box as marked in fig. A.1; *max* the maximum value in the box.

Mach	Run ID	Equip. $E_{0.95,U}$			Slip $E_{0.95,U}$		Total inst. $E_{0.95,U}$	
		fac	avg	max	avg	max	avg	max
0.48	V170	0.28	0.76	0.26	1.32	2.59	1.34	2.60
0.59	V171	0.29	0.39	0.24	1.21	2.59	1.23	2.60
0.69	V174	0.29	0.38	0.24	1.22	2.66	1.24	2.68
0.79	V164	0.29	0.32	0.24	1.26	2.83	1.28	2.84
0.90	V165	0.30	0.36	0.24	1.69	3.44	1.70	3.46

The flow field related to the equipment-based 95% confidence interval for the current Mach 0.8-case is provided in fig. A.1 a). The similarity between the uncertainty estimate in the field and the flow field is no surprise if the linear dependency shown above is taken into consideration. The maximum equipment-related uncertainty is in the range of $E_{0.95,U}(\text{equipment}) \sim 0.3\%$. Figure A.1 contains another uncertainty field which is addressed next.

A.2.1.2 Particle Dynamics

The particle slip is exemplarily approximated in the following for the current Mach 0.8-case (V164) according to section A.1.1.2. The instantaneous flow field received from the PIV measurements are used in eq. (A.7) to approximate the slip of the particles. The spatial acceleration in the instantaneous flow field in the streamwise and radial direction, i.e. $\partial U_p/\partial x_P$ and $\partial U_p/\partial y_P$, respectively, are determined by means of a least square differential operator. With respect to the particle size, the manufacturer (see section 2, Methods) specifies $20\,\text{nm}$ as median primary particle size. In the frame of the particle dynamics consideration, the more conservative number based $d_{P,50n} = 0.23\,\mu\text{m}$ is used with a particle density of $\rho_P = 3800\,\text{kgm}^{-3}$. Lazar *et al.* [8] also provides an equation to determine the fluid viscosity μ_F as function of the velocity in the flow field, but the viscosity is conservatively approximated as being constant over the flow field with the free stream viscosity $\mu_F = \mu_{F,\infty} = 1.63 \cdot 10^{-5}\,\text{kgm}^{-1}\text{s}^{-1}$ (for $T_\infty = 255\,\text{K}$) for the Mach 0.8-case (V164).

The result is shown in fig. A.1 b) and it can be seen that the particle response is mostly affected in the shear layer. Obviously, this is where the acceleration is largest and the particles correspondingly exhibit the largest slip with respect to the fluid. For comparisons with the other investigated Mach numbers, the relative slip-related uncertainty was spatially averaged (within the box) and the results of which are listed in table A.2. The maximum upper bound for the other cases is in the range of 3%.

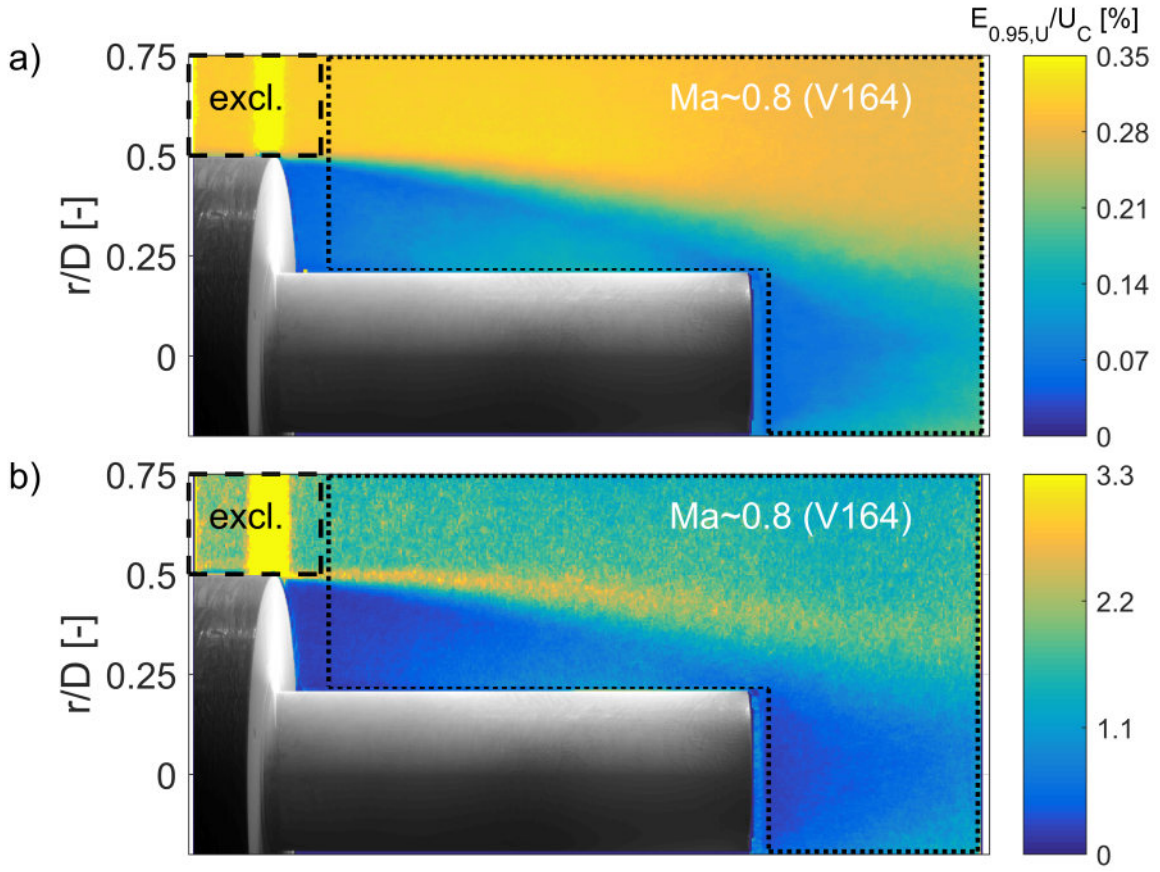

Figure A.1: Equipment-related (a) and particle-slip-related (b) in the flow field for the Mach 0.8-case (V164).

A.2.1.3 Total Instantaneous Uncertainty

The total instantaneous uncertainty, meaning the total uncertainty for one evaluated raw image set, for the wake flow at Mach 0.8 (V164) is provided in fig. A.2. This correspond to the combination of the equipment- and particle response-related uncertainty according to eq. (A.1). The total instantaneous uncertainty is largest in the shear layer. On average (box), the upper 95% confidence bound of the total uncertainty amounts to about 1.3% while the largest values are found in the shear layer to be in the range of 3% for the Mach 0.8-case. The total instantaneous uncertainties are equally listed in table A.2.

A.2.2 Confidence Levels of Mean and Fluctuation Statistics

The uncertainty regarding the statistics is inversely proportional to the square root of the number of samples N. Since $N = 345$ images have been captured, the uncertainty of the mean and turbulent velocity of the wake flow is then given by eq. (A.12) and eq. (A.13).

$$E_{0.95,\overline{U}}(\text{sampling}) \overset{\text{N=345}}{=} \pm 0.106 \cdot \sqrt{\overline{U'^2}} \tag{A.12}$$

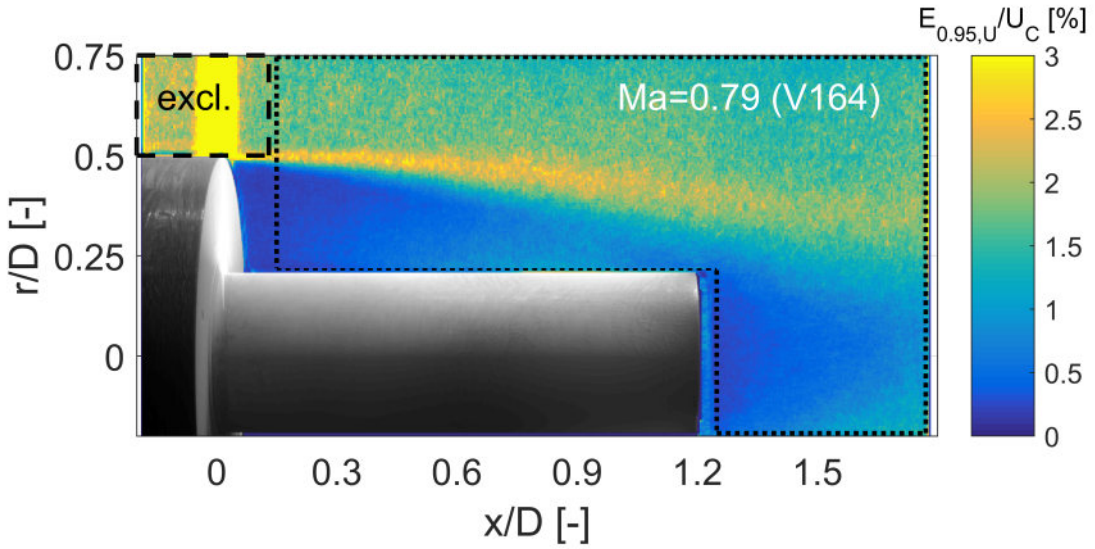

Figure A.2: Accumulated total uncertainty distribution (upper bound) of the instantaneous error sources such as introduced by the equipment and the particle response for one instantaneous sample for the Mach 0.8-case (V164).

Table A.3: Overview of the sampling-induced 95% uncertainties of the mean and turbulent velocity of the wake flow. The abbreviation *avg* denotes the spatially averaged uncertainty in the box as marked in fig. A.3; *max* the maximum value in the box. Uncertainties are given in percent.

Mach	Run ID	Mean vel. $E_{0.95,\overline{U}}$		Turb. vel. $E_{0.95,\sqrt{\overline{U'^2}}}$		Total vel. $E_{0.95,\overline{U}}$	
		avg	max	avg	max		
0.48	V170	± 0.87	± 1.71	± 0.66	± 1.19	1.69	2.61
0.59	V171	± 0.80	± 1.76	± 0.58	± 1.11	1.56	2.62
0.69	V174	± 0.79	± 1.78	± 0.56	± 1.20	1.56	2.73
0.79	V164	± 0.79	± 1.95	± 0.58	± 1.23	1.60	2.98
0.90	V165	± 0.81	± 1.94	± 0.60	± 1.27	2.00	3.43

$$E_{0.95,\sqrt{\overline{U'^2}}}(\text{sampling}) \overset{\text{N=345}}{=} \pm 0.106 \cdot \sqrt{\frac{\overline{U'^4} - \overline{U'^2}^2}{4\overline{U'^2}}} \tag{A.13}$$

The application of which on the flow field results in the statistics-related uncertainty distribution as shown in fig. A.3. The upper graph shows the statistical 95% uncertainty for the mean velocity, while the bottom graph shows the same for the turbulent velocity. For determination of both values, the turbulent velocity is the dominant parameter. Thus, the uncertainty is highest in the vicinity of the shear layer. The average and the maximum values (box) for the investigated Mach numbers is again collected and listed in table A.3. One finds an average sampling error (in box) in the range of $\pm 0.9\%$ and $\pm 0.7\%$ for the mean and turbulent quantity, respectively; at max (in box), it is $< 2\%$ and $\leq 1.3\%$, respectively.

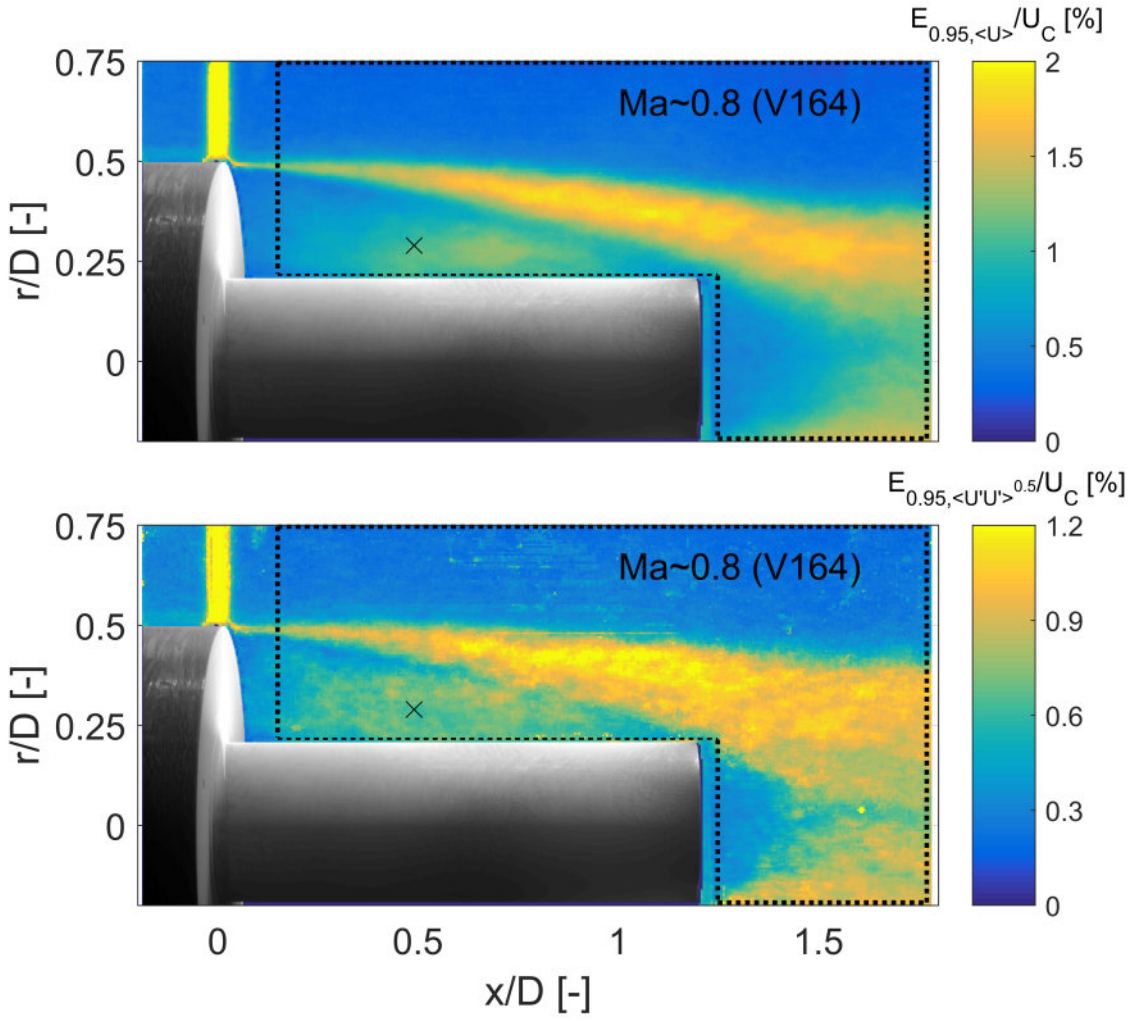

Figure A.3: Sampling-related uncertainty field for the mean velocity (top) and the turbulent velocity (bottom) for the Mach 0.8-case (V164). The point marked with a cross denotes a position, which is used in the following for the exemplary assessment of the sampling error (fig. A.4) and of the cross-correlation quality (fig. A.10). Its location was randomly selected and is in the recirculation bubble at $[x,r]/D = [0.47,0.3]$.

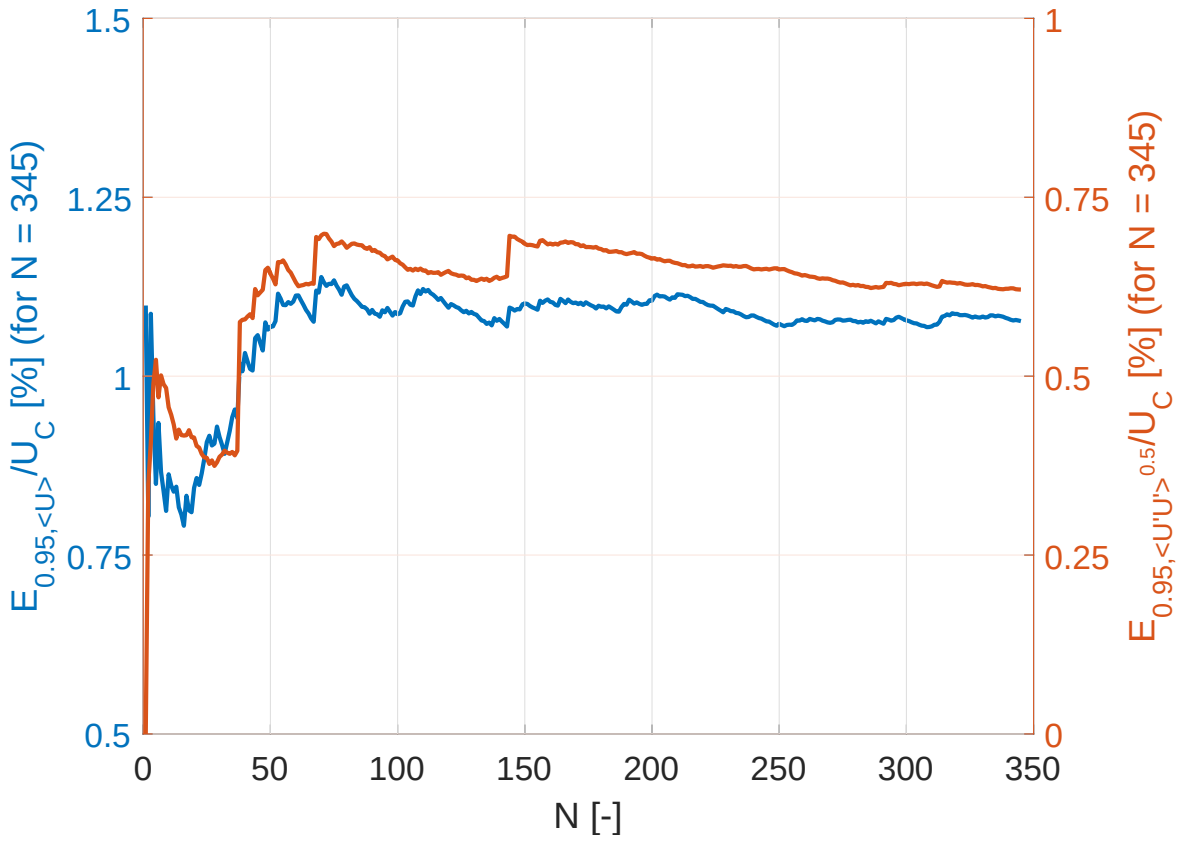

Figure A.4: Sampling error convergence for the representative point defined in the caption of fig. A.4.

The sampling error decreases with increasing sample size N. A large number of samples is obviously then desired. In the frame of the current study, 345 images were taken, which rises questions regarding the convergence of the solution. The evolution of the sampling error according eq. (A.12) and eq. (A.13) is shown in fig. A.4 for the mean and turbulent velocity. The inherent term $1/\sqrt{N}$ regarding sample number term was left at a constant value for $N = 345$ to isolate the curve from the converging trend induced by that term. In other words, a constant error level then evidences a sample-number-independent convergences of the sampling error. This can be seen for both curves at their tails, thus the results are presumed to be sufficiently converged.

A.2.3 Total Uncertainty

The total uncertainty of all considered error sources accumulates to the the distribution as given in fig. A.5. Correspondingly, the various error sources have been combined according to eq. (A.1). This graph confirms the previous observation that the uncertainty is the highest in the region where the flow is most turbulent, speaking of the shear layer. A spatially averaged and a maximum value for the data in box is provided in table A.3.

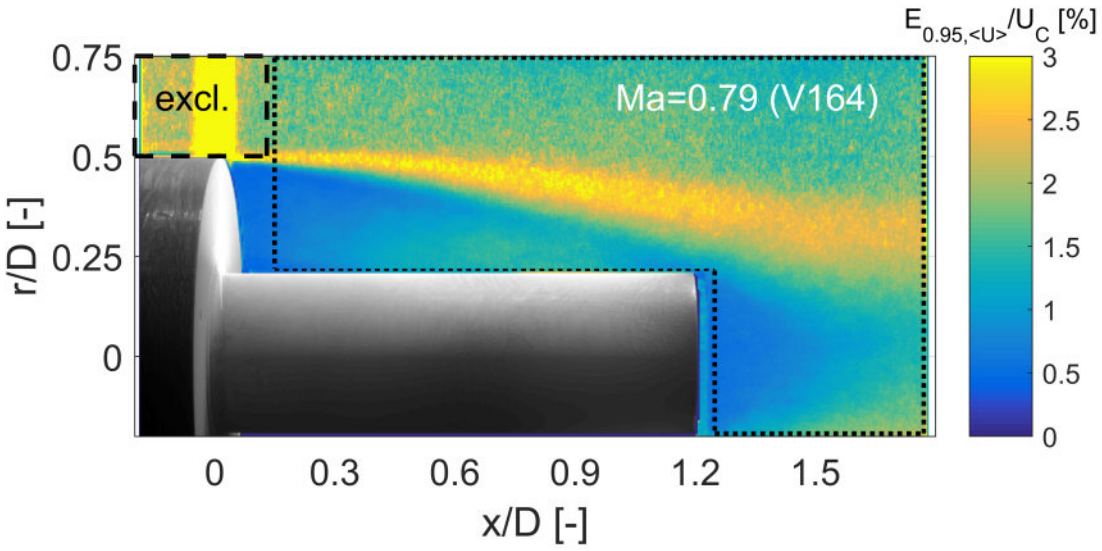

Figure A.5: Accumulated total uncertainty distribution (upper bound) of all considered error sources for the Mach 0.8-case (V164).

A.2.4 Uncertainty for Vorticity Thickness

The uncertainty for the vorticity thickness is assessed in the following. For that purpose, the vorticity thickness is repeated in eq. (A.14) where the maximum velocity gradient $(\partial u/\partial r)_{max}$ is abbreviated with the variable a. As before, u_{max} corresponds to the incoming free-stream velocity u_∞ and u_{min} to the maximum upstream velocity in the recirculation bubble. Under the assumption that the error sources are independent, this results in the error propagation formula as given in eq. (A.16).

$$\delta_\omega = \frac{u_{max} - u_{min}}{(\partial u/\partial r)_{max}} \rightarrow \delta_\omega = f(u_{max}, u_{min}, a) \qquad \text{with: } a = (\partial u/\partial r)_{max} \tag{A.14}$$

$$E_{0.95,\delta_\omega} = \sqrt{\left(\frac{\partial \delta_\omega}{\partial u_{max}} \cdot E_{0.95,u_{max}}\right)^2 + \left(\frac{\partial \delta_\omega}{\partial u_{min}} \cdot E_{0.95,u_{min}}\right)^2 + \left(\frac{\partial \delta_\omega}{\partial a} \cdot E_{0.95,a}\right)^2} \tag{A.15}$$

$$E_{0.95,\delta_\omega} = \sqrt{\left(\frac{1}{a}\right)^2 \cdot (E^2_{0.95,u_{max}} + E^2_{0.95,u_{min}}) + \left(-\frac{u_{max} - u_{min}}{a^2}\right)^2 \cdot E^2_{0.95,a}} \tag{A.16}$$

Except for uncertainty regarding the velocity gradient $E_{0.95,a}$ all other variables are known. The local uncertainty regarding the velocity $E_{0.95,u_{max}}$ and $E_{0.95,u_{min}}$ are shown above as field data and is extracted from there. Thus, the uncertainty regarding the velocity gradient must be determined, which was addressed by means of synthetic images. *PIVview* is equipped with a synthetic image generator capable of generating raw PIV images. The corresponding uncertainty was determined by opposing the input value to the evaluated output values.

The uncertainty approach above does not incorporate a bias introduced due to sub-grid filtering. Sub-grid filtering effects are well-known in PIV measurements. The motions of several particles in one interrogation window are combined and reduced to one single trajectory representing a filtered motion of all particle motions inside the interrogation window. Among neglecting highly turbulent particle motions, it also affects the ability to resolve motions with strong velocity gradient changes. A archetypical velocity gradient change is given by a step function where the velocity experiences a sudden, step-like change. In nature, this is given by a normal shock. Due to the spatial extent of the interrogation window, the PIV approach introduces an artificial smoothing and flattening of the velocity gradient. This smoothing effect is dependent of the particle image size and on the spatial extent of one interrogation window. For relatively small particles image size, meaning a particle image diameter in the range of $2\,\mathrm{px}$, a step function is approximately smoothed over the extent of the interrogation window [11].

To a lesser extent, relatively strong gradients are also present in the shear layer that separates from the main body of the configuration under investigation. In other words, the velocity is notably smoothed over the shear layer if its thickness is in the order of an interrogation window. This must be considered for the velocity gradient which is required as input for the determination of the vorticity thickness used in submitted paper. In the following, the velocity gradient in the overlap region between field of view FOV1 and FOV2 is assessed to explain the differences in the corresponding axial vorticity thickness evolution.

The velocity gradient for the overlap region is provided in fig. A.6 for the Mach 0.8-case (V117 and V164) and it can be seen that the two differ. The gradient for FOV1 is smaller, which is, as elaborated above, due the coarser resolution of the shear layer and the inherent smoothing effect. In detail, only 3.9 or 12.5 grid cells capture the velocities in the shear layer at $x/L_r = 0.15$ without and with oversampling, respectively. Note that the term 'without oversampling' refers to the fact that the results at the individual grid points are independent and no information is shared with the neighboring grid points. In summary, the resolution of the shear layer appears to be underresolved below $x/L_r = 0.2$ for FOV1 . The question now is if the higher resolved FOV2 actually captures the 'true' gradient.

This is rather difficult to assess. An indication is provided by the approximating the gradient over the shear layer. The current data set show in in fig. A.6 suggests a velocity gradient of about $260000\,\mathrm{s}^{-1}$ at $x/L_r = 0.05$ (see arrow). In other words, the incoming velocity of about of $250\,\mathrm{ms}^{-1}$ roughly adjusts within a shear layer thickness of $1\,\mathrm{mm}$ to the predominant velocity on the other side of the shear layer, which is estimated here to be at the order of $0\,\mathrm{ms}^{-1}$. This appears plausible taking into account the thinning of the upstream boundary layer due to the acceleration of the edge of the base. Further, at this location, the shear layer exhibits a thickness of about $0.9\,\mathrm{mm}$, which is resolved by approximately 18 grid points if oversampled with an overlap of 75% (as done here) and with 5 grid points without oversampling. Farther downstream, the spatial resolution over the shear layer increases for FOV2 due to the increasing shear layer thickness. At $x/L_r = 0.15$, 37 oversampled and 10 independent grid points are located in the shear layer for FOV2. In other words, the velocity gradient appears to be sufficiently resolved at that axial location; especially in the region of the maximum velocity gradient where the changes are moderate.

Figure A.6 also contains the streamwise evolution of the ratio between both maximum velocity gradients. It can be seen that the ratio between both converges with increasing distance from

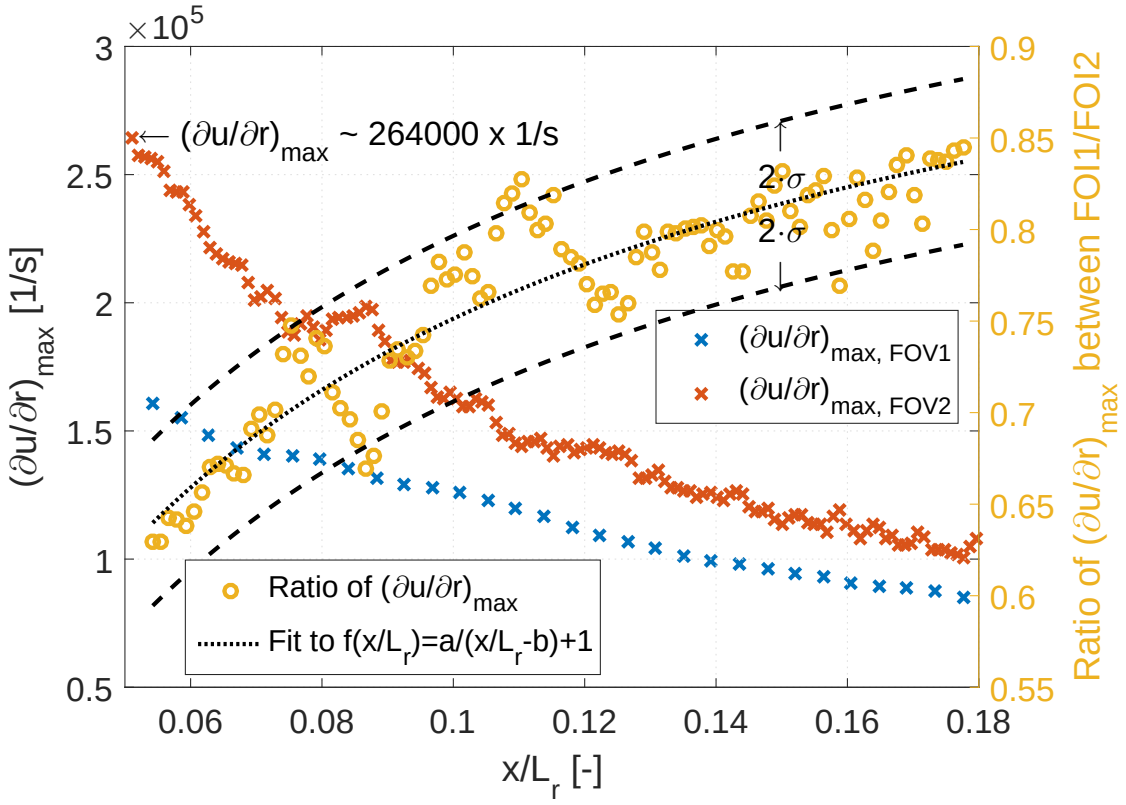

Figure A.6: Maximum velocity gradient for the two field of views, FOV1 and FOV2 and the ratio between the two gradients as function of the locality in the axial direction for the Mach 0.8-case (V117 and V164). The fit result of the ratio to $f(x/L_r) = a/(x/L_r - b) + 1$ is given with $a = -0.037 \cdot 1/s$ and $b = -0.0478$; the standard deviation between the measured and fitted results amounts to 0.023.

the point of separation. Nevertheless, at the end of the overlapping zone at $x/L_r = 0.18$, the lesser resolved FOV1 result has only reached about 80% of the results by FOV2. Thus, based on this trend, it can be assumed that the deviation is still persistent in the region where only FOV1 results are available. To take this into account, a fit was determined for convergence trend. Obviously, the fit features a deviation from the measurements, which is quantified by means of the standard deviation σ. Next, the trend with $2 \cdot \sigma$ is incorporated as bias in the error bar of the graph for the discussion of the vorticity thickness in fig. A.7. The corresponding lower bound is shifted by the fit regarding the velocity gradient bias.

A.2.5 Side Notes to the Image Analysis

The previous section pursued the objective to provide quantitative uncertainty levels for the velocimetric results. The current section focuses on rather qualitative considerations. Qualitative since these considerations cannot not directly be fed into the velocity uncertainty assessment. Nevertheless, it is believed that they provide valuable insights and rule out some concerns. In particular, aspects to the seeding density, to the signal-to-noise ratio of the cross-correlation results and to peak-locking are presented.

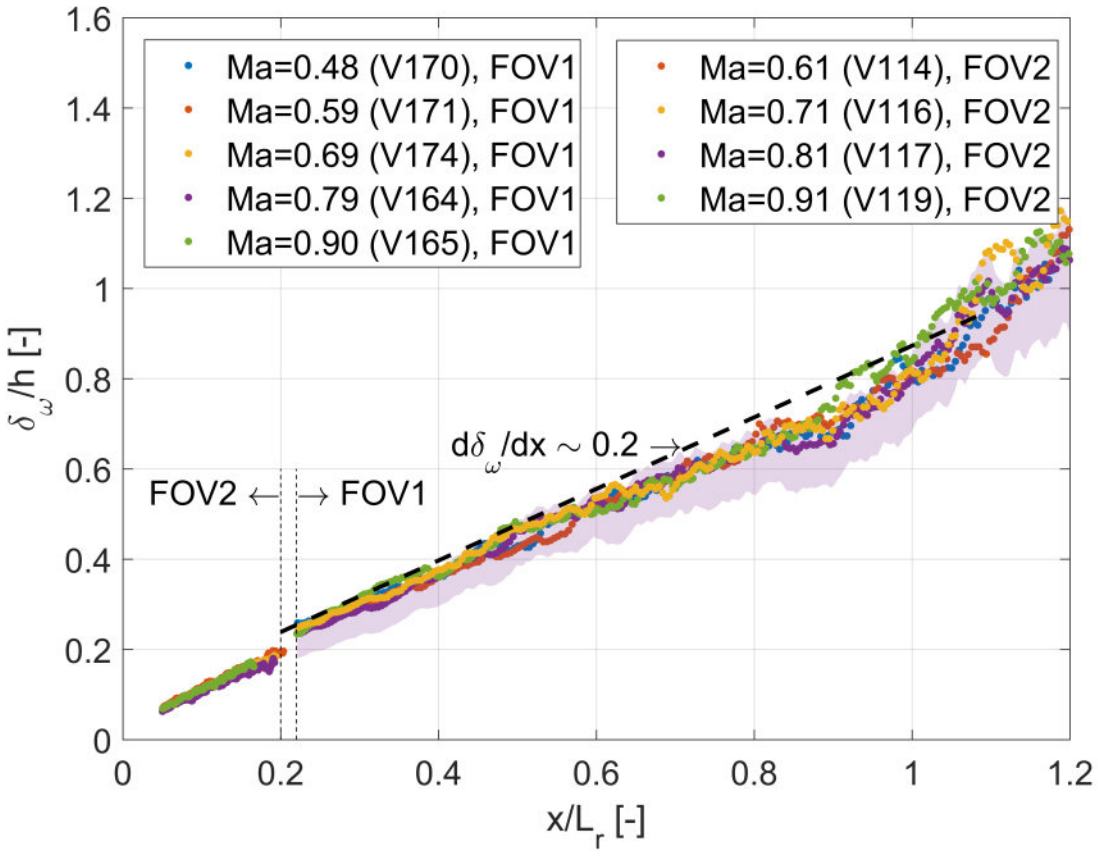

Figure A.7: Streamwise vorticity thickness evolution for the investigated Mach numbers. The results of both field of views are shown, meaning FOV1 and FOV2. The shading exemplarily shows the uncertainty bounds for the Mach 0.8-case (V164).

A.2.5.1 Wake Flow Seeding

Seeding of a near-wake flow can be an issue. Especially in hypersonic flows, particles coming from the upstream direction feature a similarly high velocity as the fluid itself, thus the particles do not necessarily tend to intrude the recirculation bubble. Moreover, the particles inside of recirculation center tend to get ejected for the same reason, which is the high velocity or high momentum. Thus, the question of seeding density in the near-wake is a justified one.

A randomly-picked raw PIV image, which is depicted in fig. A.8, however proves that the opposite is the case. The recirculation region exhibits a high seeding density, while the ambient flow above $r/D > 0.6$ is more sparsely seeded. To encounter the impression that there are insufficient particles in that region it shall be mentioned that the illumination in the near-wake just dominates the image due to the local seeding density. For most images, there are still enough particles in the ambient flow to execute PIV evaluations. Focusing on the seeding in the recirculation bubble again, it can be stated the recirculation bubble actually acts in favor for the PIV measurements. An opposition of various double images showed that a good amount of particles seems to be locked inside the bubble providing a homogeneously distributed seeding density over time.

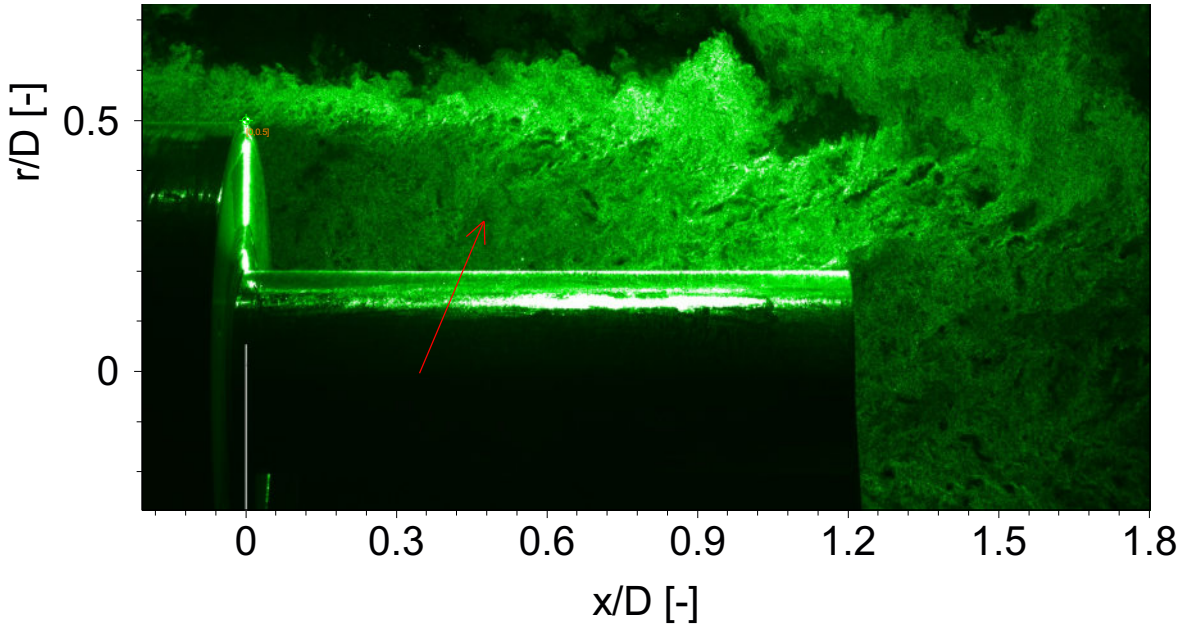

Figure A.8: First raw image of double PIV recording. The arrow marks the representative point defined in the caption of fig. A.4. Data stems from the Mach 0.8-case (V164).

This statement is supported by the rms (root mean square) values of the pixel intensity over the samples given in fig. A.9. It shows that the highest intensity fluctuations occur outside of the recirculation bubble. This is conform with observations made for individual raw images which show that the particle density varies over time in that region, while it remains rather constant inside the recirculation bubble.

A.2.5.2 Signal-to-Noise Ratio of the Correlation Plane

Raw double images are the main input for the PIV evaluation. PIV evaluation essentially consists of a cross-correlation between interrogation windows taken from first image (*image A*) and the second image (*image B*). The result of which is the cross-correlation plane. This is provided in fig. A.10 for the randomly-selected, representative point in the recirculation bubble to visualize its corresponding peak signal strength (for exact location, see arrow in fig. A.8, for instance). The figure additionally shows the input interrogation windows of image A and B. It can be seen that despite not resolving individual particles due to the high density seeding, the signal-to-noise ratio is strong, and therefore the location of the peak is less ambiguous.

Generally, a high signal-to-noise ratio with respect to the correlation plane can be found. This can be seen in the signal-to-noise ratio field exemplarily shown in fig. A.11 for the first double image of the current measurements under consideration (V164). This is an indicator for a reliable determination of the displacement.

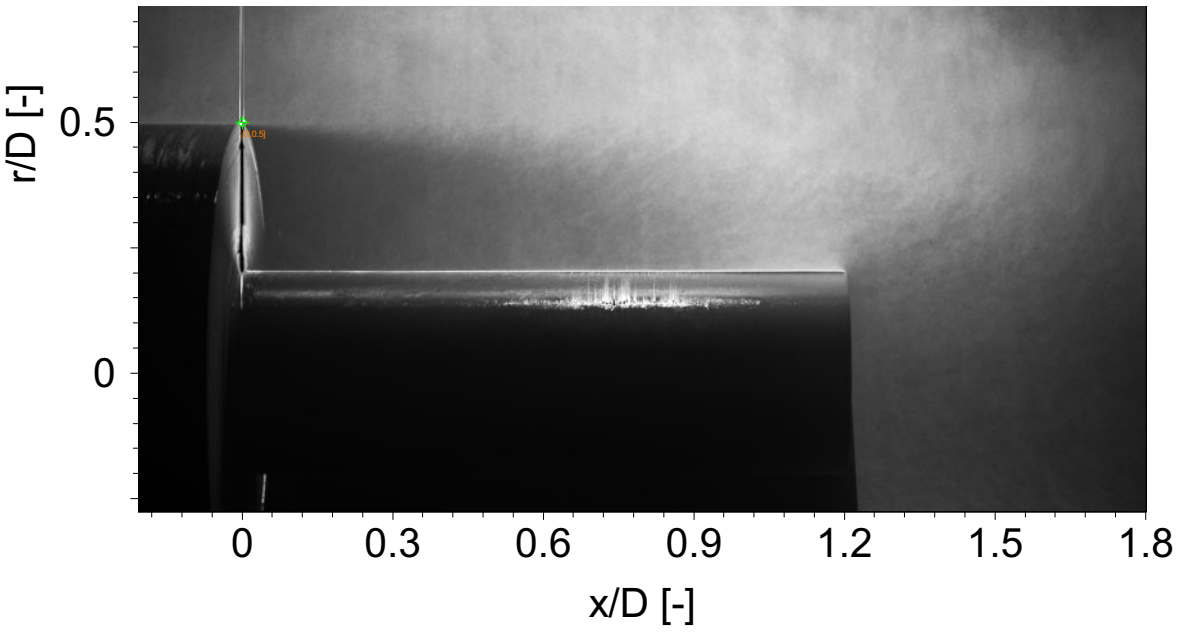

Figure A.9: rms of pixel intensity over the 345 raw PIV images. Data stems from the Mach 0.8-case (V164).

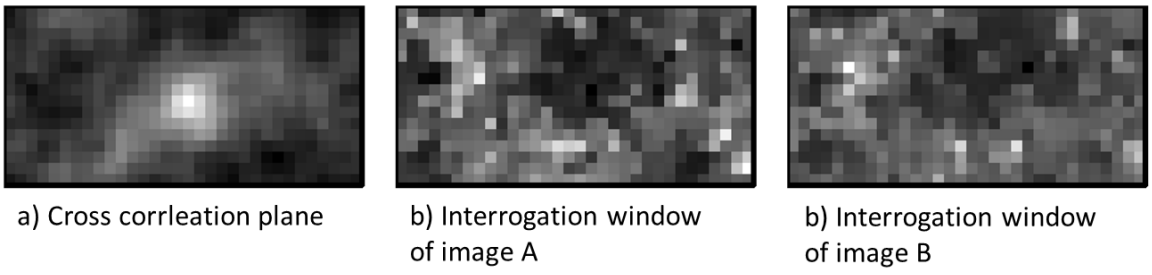

Figure A.10: Exemplary cross-correlation evaluation of an interrogation window located at the representative point defined in the caption of fig. A.4. Data stems from the Mach 0.8-case (V164).

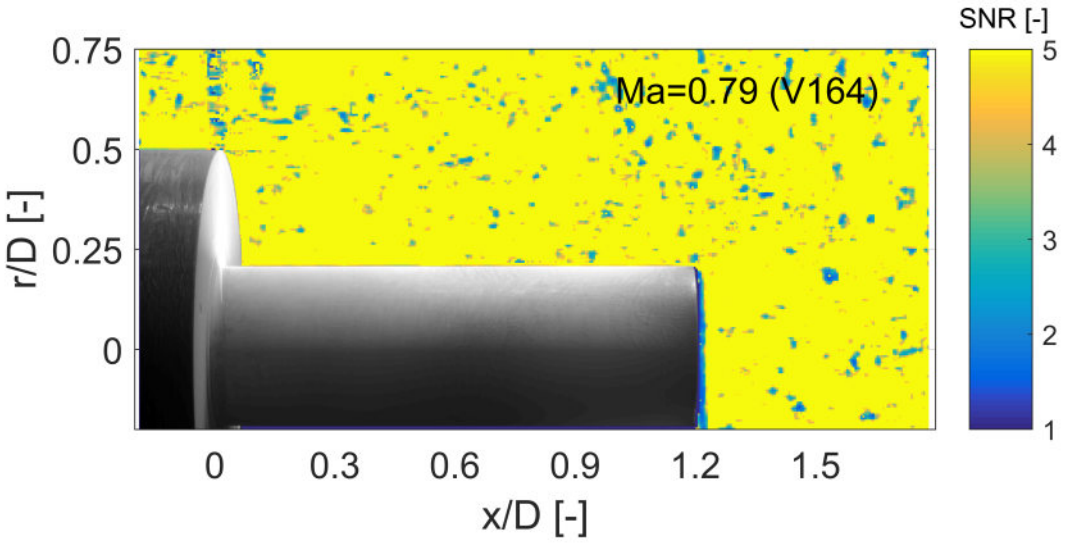

Figure A.11: Signal-to-noise ratio in the cross-correlation plane of the first double image of the Mach 0.8-case ($V164$).

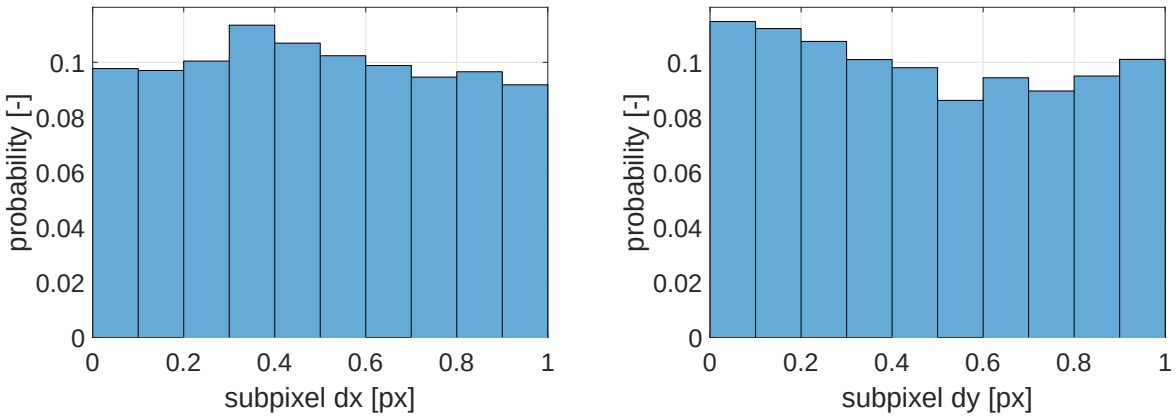

Figure A.12: Subpixel displacement of an instantaneous PIV result in the near-wake shown with the objective to rule out peak-locking. Data stems from the Mach 0.8-case (V164) and is extracted from the wake region.

A.2.5.3 Peak Locking

Peak-locking is an effect which describes the bias of the displacement towards integral values. This effect occurs if the particles become too small such that the cross-correlation 'locks' the displacement into individual pixels. For the case at hand though, this appears not to be the case. First, the particles image covers more than just one pixel, and second, the seeding density is relatively high. Correspondingly, the displacement in the subpixel range is relatively equally distributed, which is shown infig. A.12. Consequently, peak-locking is ruled out here.

Table A.4: Summary of equipment uncertainty parameters for the Mach 0.8-case (V117) focusing on the boundary layer flow.

Category	Parameter	Description	y_i	$E_{0.95,i}$
Calibration	l	Calibration scale physical length	31.2 mm	10 μm
	L1	Calibration scale image plane length	1600 px	1px
	L2	Image distortion due to aberrations	1600 px	0 px
	λ	Distance from calibration scale to lens	260 mm	0.5 mm
Timing	Δt	Combined t1 and t2	0.77 μs	2.6 ns

A.3 Uncertainty Analysis for the Boundary Layer Flow

Despite the most likely interesting aspects that could be investigated more deeply, the results of field of view FOV2 are mainly concerned to provide information to the incoming flow, more specifically to the boundary layer, and to back the results for the vorticity thickness. Due to this reason and since the uncertainty considerations for the wake flow above is more elaborate, the following uncertainty considerations are limited to the essentials.

The various uncertainties are collected in table A.5 and table A.6. Both tables list averaged and maximum values extracted from a box where the boundary layer has been determined in the frame of the submitted paper. This was at $x/D = -0.15$. The box reaches for all Mach numbers from the upper end of the boundary layer δ_{99} to $0.1 \cdot \delta_{99}$ and its width extends from $-0.175 \leq x/D \leq -0.125$. Further, the box is visualized in all uncertainty distributions presented in the following. As an example, it shall be referred to fig. A.13.

A.3.1 Confidence Levels of Instantaneous Samples

In the following, the uncertainty sources influence the instantaneous results are presented.

A.3.1.1 Equipment

The same approach is applied for the determination of the boundary layer flow as for the wake flow. Table A.4 lists all the input parameters associated with the corresponding scaling magnification of field of view FOV2 and with the timing accuracy. This results in an equipment-based uncertainty as given by eq. (A.17). For the boundary layer flow, the uncertainty introduced by the *jitter* of the laser system becomes more dominant, which is simply an effect of the delay time reduction. An overview to the eqipment-related uncertainty and to other uncertainties is provided in table A.5 for the various investigated Mach numbers.

$$\begin{aligned} E_{0.95,U} &= U\left(\underbrace{0.10\cdot10^{-6}}_{\mathrm{l}}+\underbrace{0.4\cdot10^{-6}}_{\mathrm{L1}}+\underbrace{0}_{\mathrm{L2}}+\underbrace{3.7\cdot10^{-6}}_{\lambda}+\underbrace{11.4\cdot10^{-6}}_{\Delta t}\right)^{0.5} \\ &= 0.0039\cdot U \qquad \text{for the boundary layer flow at Mach } 0.8 \text{ (V117)} \end{aligned} \tag{A.17}$$

Table A.5: Overview of the upper bound of the 95% confidence interval for the instantaneous samples for the boundary layer flow. It is given in percent of the free-stream velocity. In detail, the table encompasses the equipment-related (*Equip.*), the particle-slip-related (*Slip*), and the total instantaneous (*Total inst.*) uncertainty for the investigated Mach numbers. For the equipment-related bound, the linear factor *fac* as determined by means of eq. (A.6) is additionally provided. The abbreviation *avg* denotes the spatially averaged uncertainty in the box as marked in fig. A.1; *max* the maximum value in the box.

Mach	Run ID	Equip. $E_{0.95,U}$			Slip $E_{0.95,U}$		Total inst. $E_{0.95,U}$	
		fac	avg	max	avg	max	avg	max
0.61	V114	0.39	0.40	0.41	1.28	1.90	1.35	1.94
0.71	V116	0.37	0.38	0.39	1.34	2.48	1.40	2.50
0.81	V117	0.39	0.40	0.41	1.77	3.18	1.82	3.20
0.91	V119	0.42	0.43	0.44	1.60	3.31	1.67	3.34

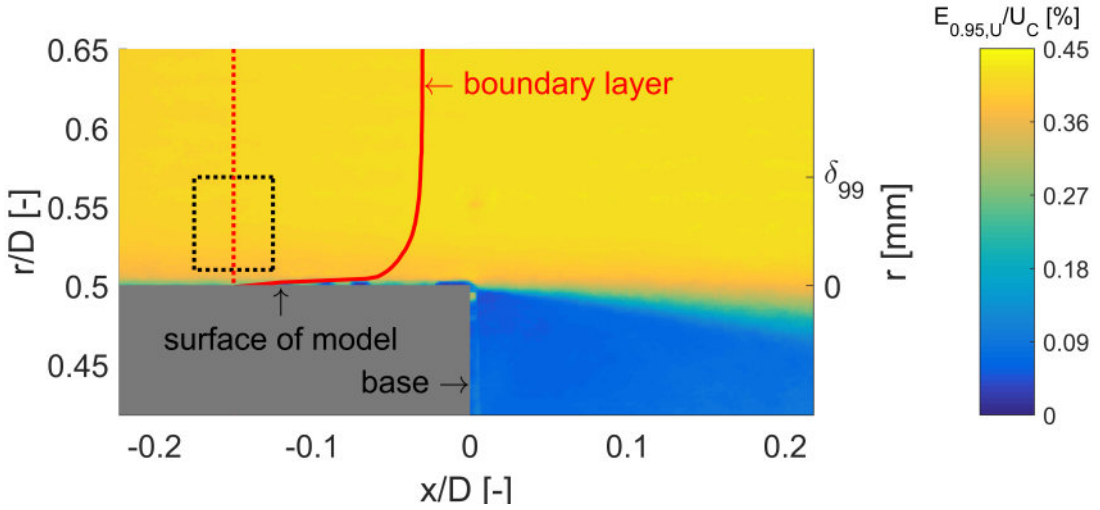

Figure A.13: Equipment-related uncertainty for the Mach 0.8-case (V117).

The equipment related uncertainty distribution is provided fig. A.13. This is the uncertainty which is linearly dependent on the local velocity, thus the distribution develops correspondingly. The maximum for the 95% uncertainty is in the range of $\pm 0.4\%$.

A.3.1.2 Particle Dynamics

Due to the absence of very strong spatial accelerations along the surface of the wind tunnel model, the uncertainty related to particle slip is moderate which is visualized in fig. A.14. Within the box, the uncertainty level for the a spatially averaged and maximum quantity is in the range of $\pm 1.8\%$ and $\pm 3.2\%$, respectively (table A.5). Stronger spatial accelerations are then found in the evolving shear layer. As a result, the particle slip also increases and values in the range of $\pm 8\%$ can be detected close to the edge of the base.

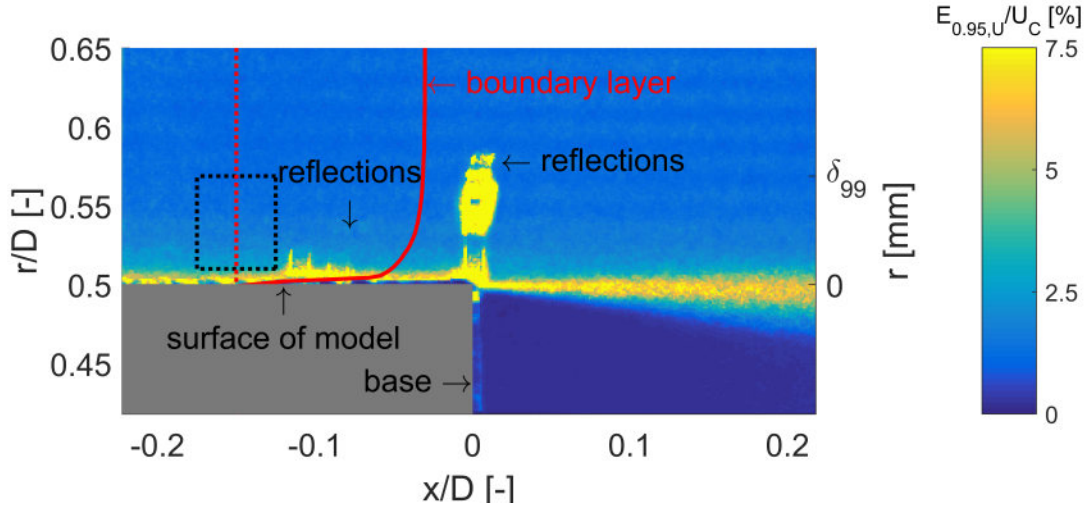

Figure A.14: Particle-related uncertainty in the flow field for the Mach 0.8-case (V117).

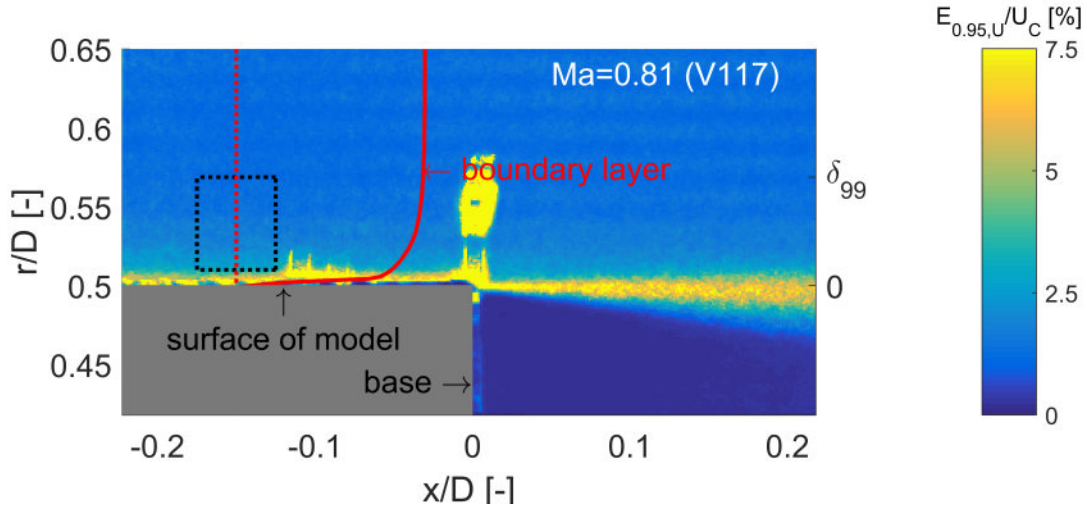

Figure A.15: Accumulated total uncertainty distribution (upper bound) of the instantaneous error sources such as introduced by the equipment and the particle response for one instantaneous sample for the Mach 0.8-case (V117).

A.3.1.3 Total Instantaneous Uncertainty

The total instantaneous uncertainty is largest in the shear layer. For the lesser affected incoming boundary layer, the upper bound amounts to a spatially averaged and maximum values (box) in the range of about $< 2\%$ and $< 3.5\%$, respectively (table A.5).

A.3.2 Confidence Levels of Mean and Fluctuation Statistics

More samples, specifically 694 samples, are available for the boundary layer measurements. As a result, the sampling related uncertainty estimation for the mean and turbulent part given in eq. (A.9) and eq. (A.10) can be rewritten as eq. (A.18) and eq. (A.19), respectively.

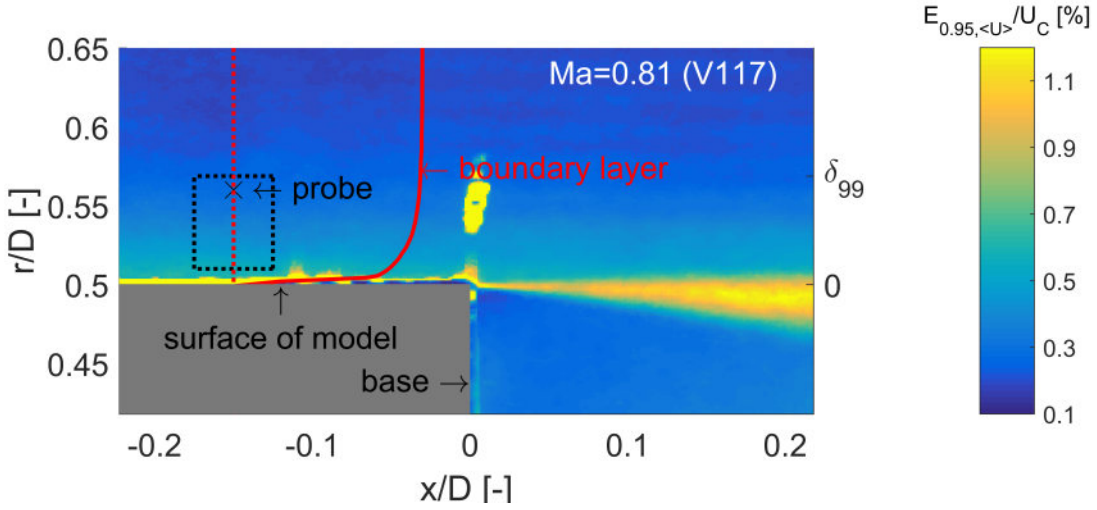

Figure A.16: Sampling-related uncertainty field for the mean velocity for the Mach 0.8-case (V117). The point marked as 'probe' is used in the frame of fig. A.18.

Table A.6: Overview of the sampling-induced 95% uncertainties of the mean and turbulent velocity of the boundary layer flow. The abbreviation *avg* denotes the spatially averaged uncertainty in the box as marked in fig. A.13, for instance; *max* the maximum value in the box. Uncertainties are given in percent.

Mach	Run ID	Mean vel. $E_{0.95,\overline{U}}$		Turb. vel. $E_{0.95,\sqrt{\overline{U'^2}}}$		Total vel. $E_{0.95,\overline{U}}$	
		avg	max	avg	max		
0.61	V114	± 0.39	± 0.59	± 0.26	± 0.35	1.40	2.03
0.71	V116	± 0.39	± 0.57	± 0.26	± 0.37	1.45	2.56
0.81	V117	± 0.39	± 0.57	± 0.27	± 0.36	1.86	3.25
0.91	V119	± 0.44	± 0.69	± 0.31	± 0.42	1.72	3.41

$$E_{0.95,\overline{U}}(\text{sampling}) \overset{\text{N=694}}{=} \pm 0.074 \cdot \sqrt{\overline{U'^2}} \tag{A.18}$$

$$E_{0.95,\sqrt{\overline{U'^2}}}(\text{sampling}) \overset{\text{N=694}}{=} \pm 0.074 \cdot \sqrt{\frac{\overline{U'^4} - \overline{U'^2}^2}{4\overline{U'^2}}} \tag{A.19}$$

The corresponding distribution for the mean and turbulent sampling uncertainty according to Benedict and Gould [2] is given in fig. A.16 and fig. A.17, respectively. The uncertainty level of both is based on the velocity fluctuation. Thus, an increased level of uncertainty can be found in the shear layer. Nevertheless, the overall level is low for both and for all Mach numbers, meaning below $\pm 0.7\%$ in the box (table A.6), and consequently, the sampling error does not contribute significantly to the total uncertainty.

The evolution of the sampling error is depicted in fig. A.18. As above, it is without updating the

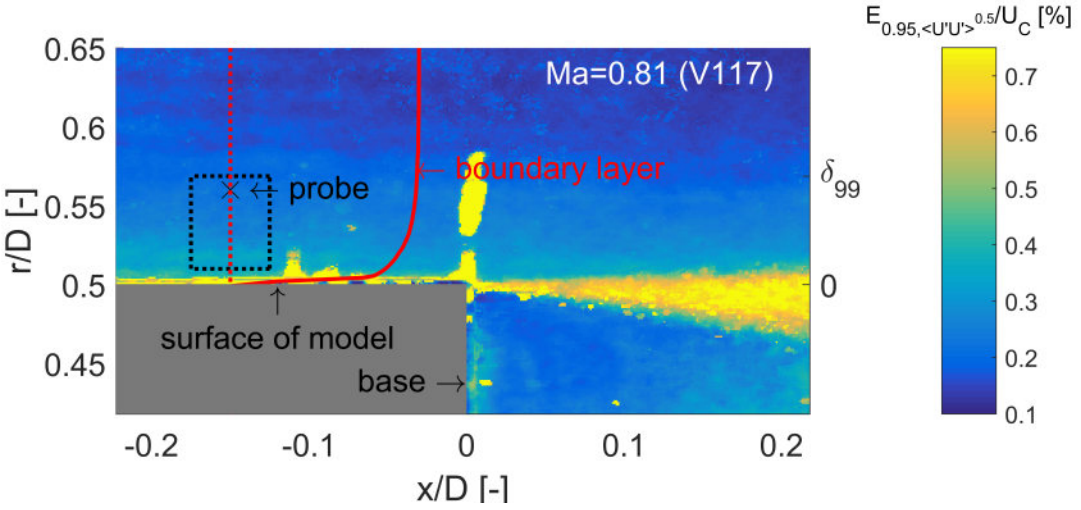

Figure A.17: Sampling-related uncertainty field for the turbulent velocity for the Mach 0.8 -case (V117). The point marked as 'probe' is used in the frame of fig. A.18.

number of samples. In other words, the number of samples for the boundary layer measurements (694 samples) is used here to isolate the tendency of the curve from the converging trend introduced by that variable. It can be seen that a threshold value is found for both, for the mean and turbulent sampling error.

A.3.3 Total Uncertainty

Last, the accumulated uncertainty for all error sources is presented as field data in fig. A.19. The distribution does not change significantly from the total instantaneous error distribution since the sampling uncertainty is rather small. In the box, it accumulates to maximum level in the range of about $< 3.3\%$. An overview to the total uncertainty for the other Mach numbers under investigation is given in table A.6.

A.3.4 Uncertainty for Boundary Layer Thickness

Above, the uncertainty in the flow field was determined. The results are used in the following to attribute an uncertainty to the boundary layer thickness by means of a Monte-Carlo simulation. The approach for one exemplary iteration is visualized in fig. A.20. The graph depicts the data points of the nominal mean velocity profile as resulted from the measurements and the deduced nominal boundary layer thickness $\delta_{99,nom}$ at 99% of the free-stream velocity. For the Monte-Carlo simulation, the original data set is superposed with normally distributed noise with the total uncertainty as determined above, e.g. of $E_{0.95,\overline{U}} = \pm 1.86\%$ for the Mach 0.8-case (V117). The average uncertainty is found appropriate here since this applies to the region close to the edge of the boundary layer. Further, note that only a section between $\delta_{95,nom} < r < 1.25 \cdot \delta_{99,nom}$ is used. Next, a curve fit to the function $u(r) = a/(r-b) + c$

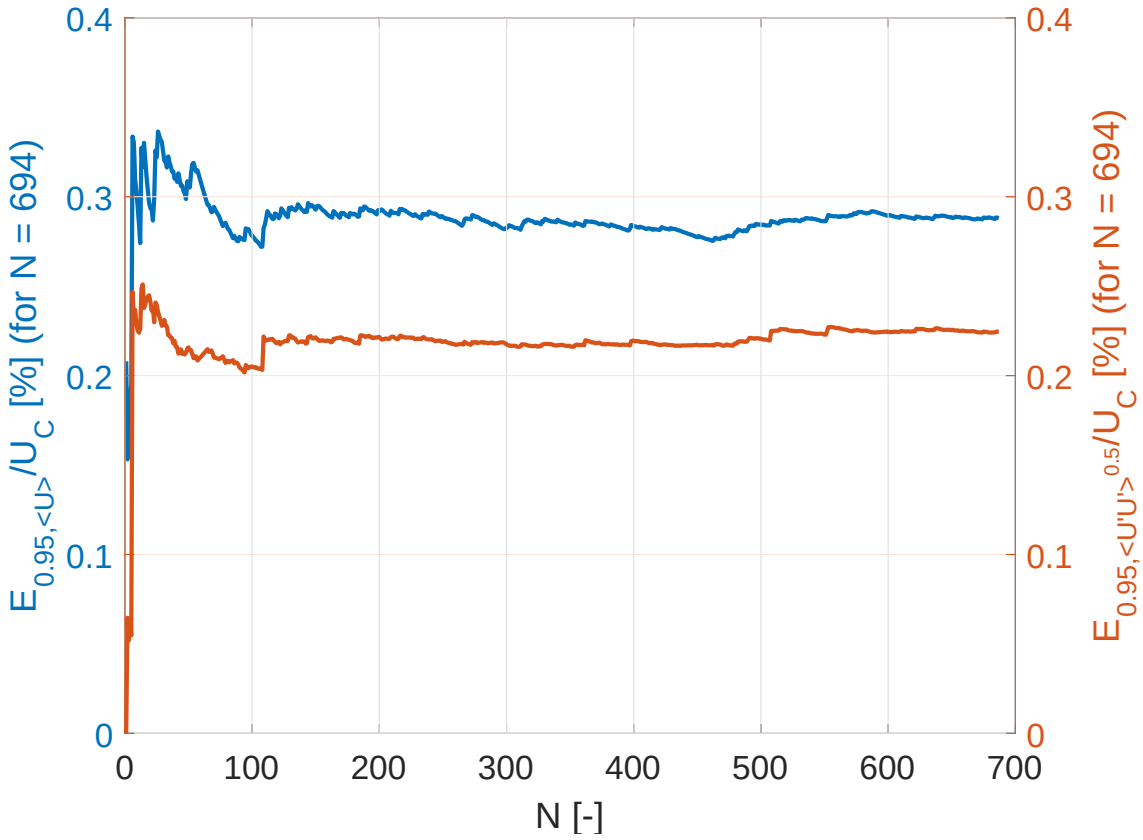

Figure A.18: Sampling error convergence for the representative point in the boundary layer at $[x,r]/D = [-0.15,0.56]$ (or 67% of the boundary layer thickness δ_{99}, which is marked in fig. A.17.

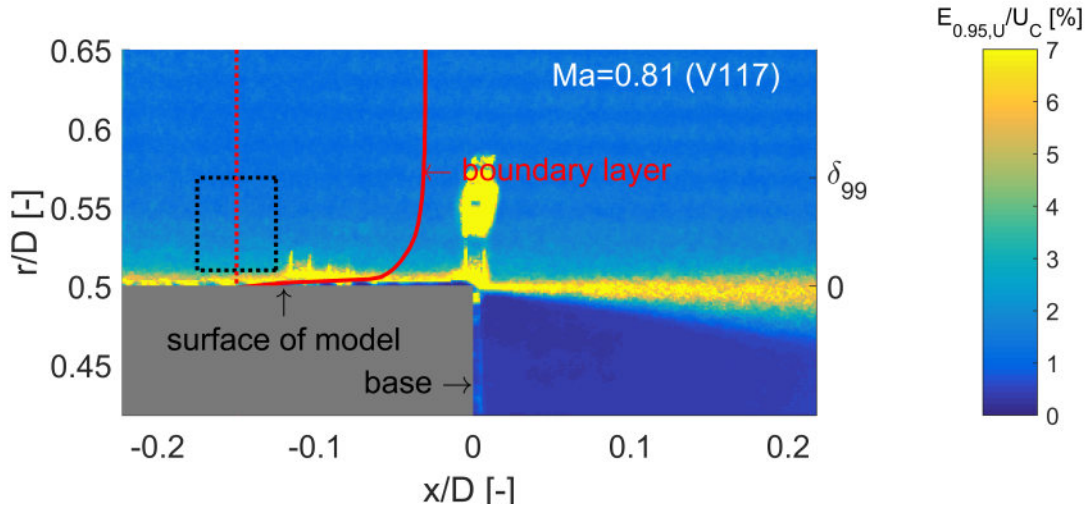

Figure A.19: Accumulated total uncertainty distribution (upper bound) of all considered error sources for the Mach 0.8-case (V117).

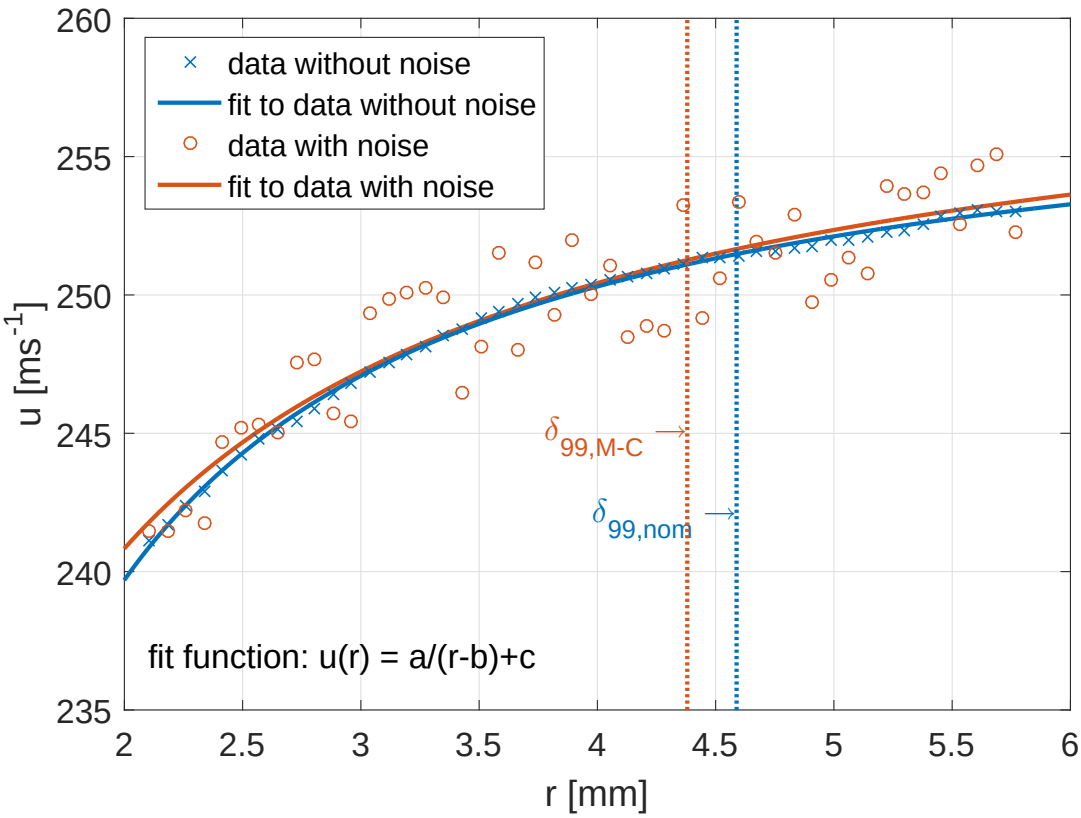

Figure A.20: Exemplary visualization concerning the uncertainty estimation of the boundary layer thickness. The uncertainty bounds of 5% are chosen here for the purpose of visualizing the Monte-Carlo simulation approach.

with the constants a, b and c is applied and the resulting boundary layer thickness $\delta_{99,M-C}$ is determined.

In total, the boundary layer thickness is determined for 10000 iterations and the result of that approach is depicted in fig. A.21 for all investigated Mach numbers. The legend contains the standard deviation of the resulting boundary layer distribution. Twice the standard deviations of the boundary layer thickness data set with noise is used as 95% confidence interval and listed in the corresponding tables in the submitted paper.

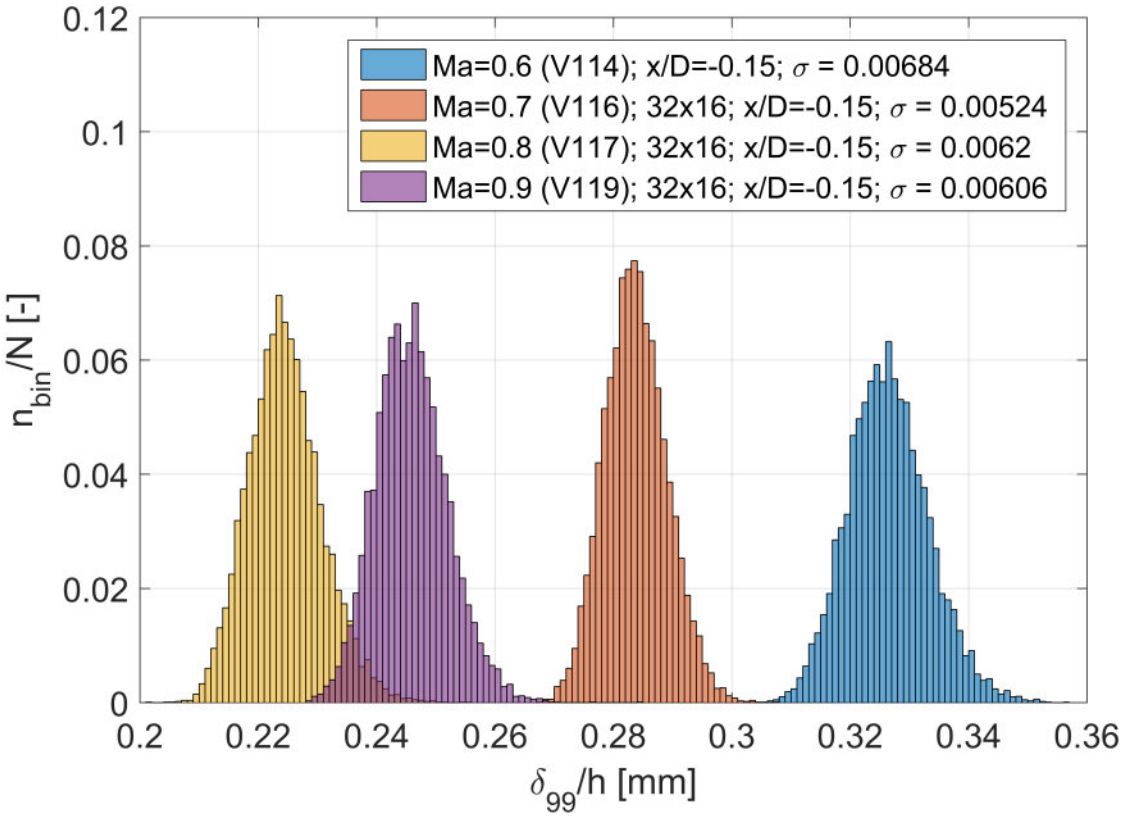

Figure A.21: Result of the Monte-Carlo simulation for the boundary layer thickness error estimation. The histogram depicts the probability distribution.

B Appendix: Additional Results

The additional results were provided in the first version of the submitted paper, but the other reviewer has asked to remove them with the argument that they do not provide new findings. The authors though believe that these results contribute to support the validity. In detail, the results in the region where both field of views overlap are useful. These are compared next. In the section afterward, profiles at locations farther downstream are presented for comparisons with the results by Weiss *et al.* [14] for the Mach 0.7-case.

B.1 Profiles Extracted from Overlapping Field of Views

The field of views for FOV1 and FOV2 exhibit an overlap, thus both results can be compared. This is true directly in the vicinity of base. At the location $x/D = 0.14$, the profiles in the radial direction of both are plotted in figs. B.1 to B.3.

The mean streamwise velocity of the two FOVs show a very good agreement (fig. B.1), which speaks for a sufficient resolution in terms of the mean velocity. On the other hand, the turbulent quantities are more challenging to resolve. The maximum turbulence intensity in the shear layer is significantly lower for the field of view which targets the wake flow (fig. B.2). In detail, the peak strength for FOV1 is $< u'u' >^{0.5} /U_C \sim 0.109$ versus 0.143 for FOV2. This becomes more severe for the Reynolds shear stress in the shear layer (fig. B.3). In conclusion, the still very narrow shear layer is insufficiently resolved at least with FOV1 at that location close to the separation. Due to the better spatial resolution, field of view FOV2 suffers less from sub-grid filtering effects in the shear layer.

Nevertheless, the turbulent quantities inside the recirculation bubble agree within the confidence interval for the sampling uncertainty for both, the turbulence intensity and the Reynolds shear stress. Additionally, the trend is similar to the unperturbed results by Weiss *et al.* [14]. Thus, it seems like the turbulent quantities in the recirculation region are sufficiently resolved.

B.2 Further Comparisons of Near-Wake Profiles with Literature

Weiss *et al.* [14] provided a large number of profiles of the wake flow at Mach 0.7 for a configuration which is equivalent to the current one. Remember that they investigated by numerical means the impact of the wind tunnel on the measurement results, which was then called perturbed (P). Unperturbed (U) corresponds to a free-flight configuration without the disturbing influence of the wind tunnel.

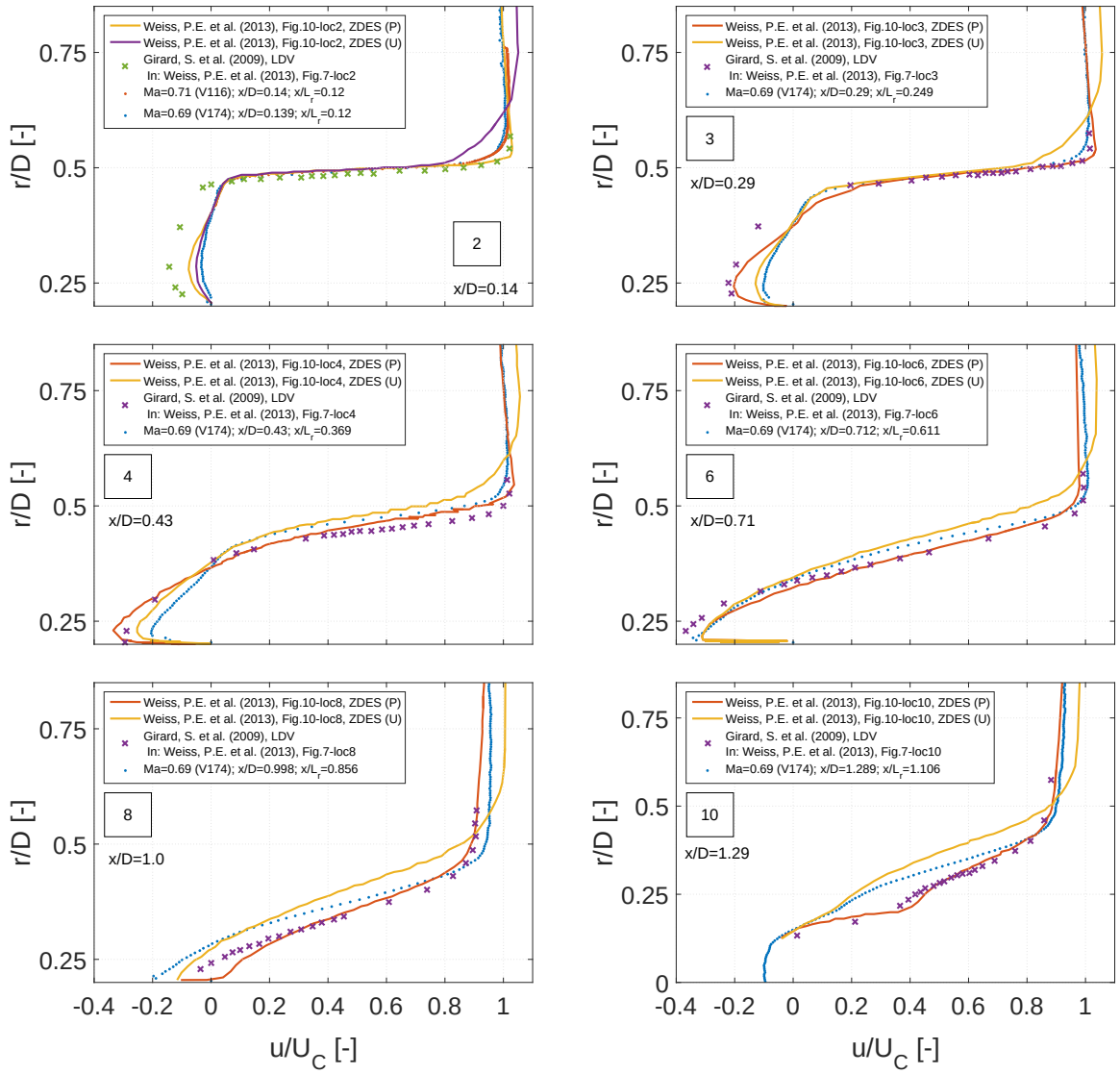

Figure B.1: Literature comparison of the mean flow velocity profiles in the wake for Mach 0.7.

The submitted paper does not contain all profiles presented in Weiss *et al.* [14], but only one at an exemplary location. Further examples of profiles with the mean velocity and with the turbulent quantities are provided here in figs. B.1 to B.3. The overall agreement with the unperturbed/free-flight case in literature appears to be surprisingly well. The term surprisingly is used here since the approach for the near-wake flow investigation is different and since there exists a difference regarding the incoming turbulence. Thus, these results evidence that the shear layer is undoubtedly under-resolved, but the dynamics in the recirculation bubble appears to be captured for the free-flight configuration.

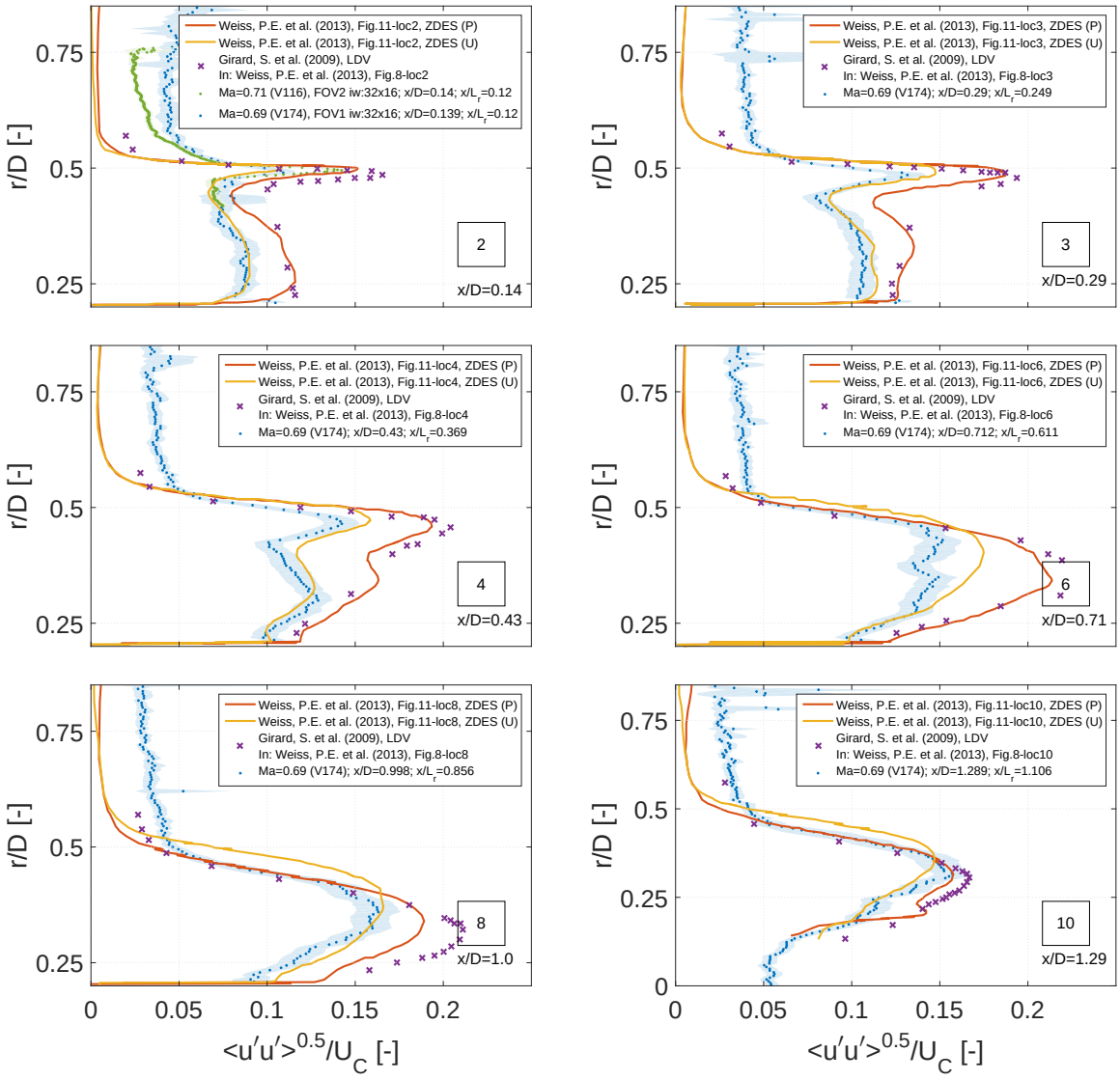

Figure B.2: Literature comparison of the axial turbulence intensity profiles in the wake for Mach 0.7.

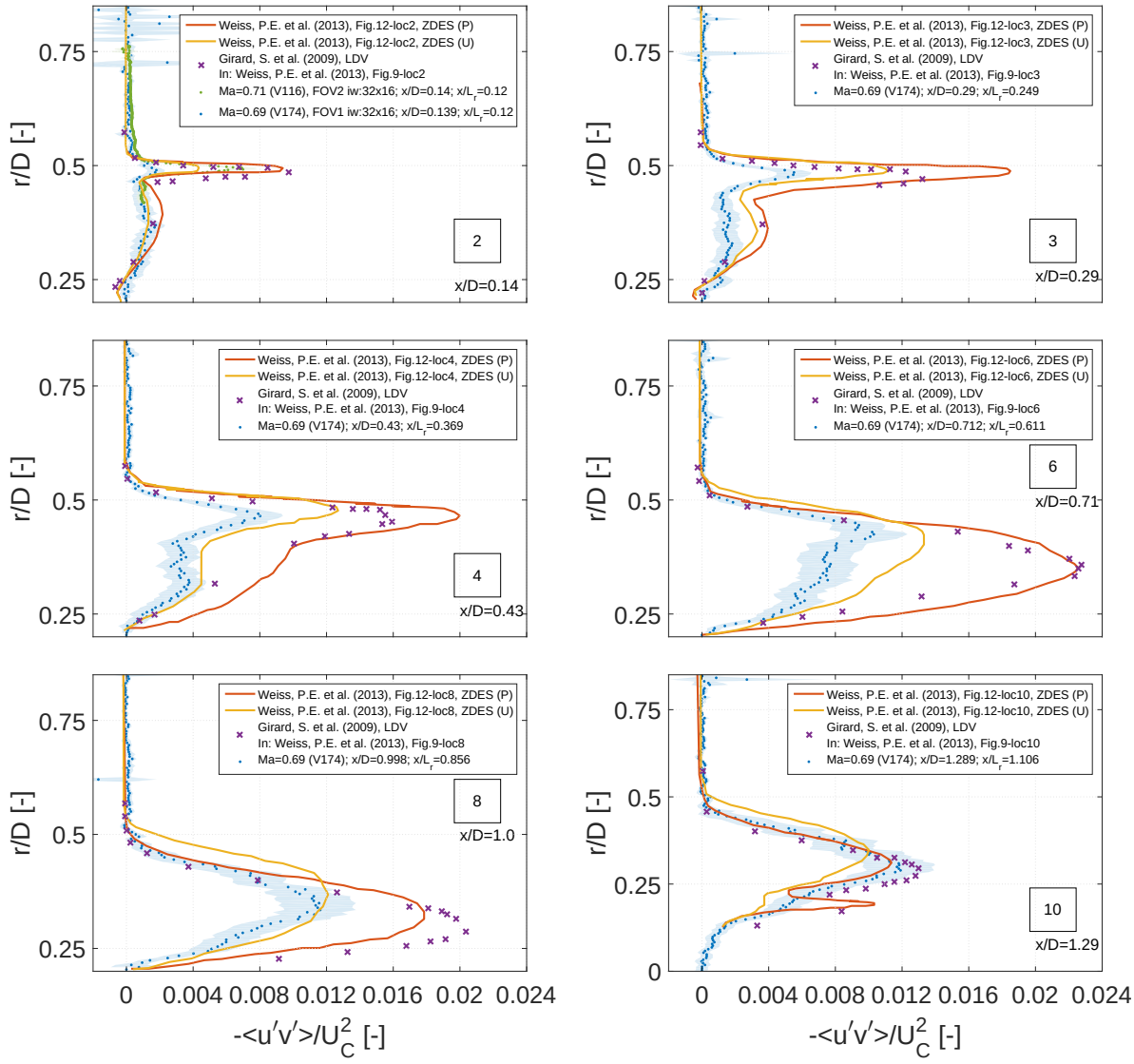

Figure B.3: Literature comparison of the Reynolds shear stress profiles in the wake for Mach 0.7.

C Bibliography

[2] Benedict, L. and R. Gould, “Towards Better Uncertainty Estimates for Turbulence Statistics”, *Experiments in Fluids*, vol. 22, no. 2, pp. 129–136, 1996.

[8] Lazar, E., B. DeBlauw, N. Glumac, C. Dutton, and G. Elliott, “A Practical Approach to PIV Uncertainty Analysis”, in *27th AIAA Aerodynamic Measurement Technology and Ground Testing Conference*, 2010, p. 4355.

[10] Raffel, M., C. E. Willert, S. Wereley, and J. Kompenhans, *Particle Image Velocimetry: A Practical Guide*. Springer, 2013.

[11] Scharnowski, S., “Investigation of Turbulent Shear Flows with High Resolution PIV Methods”, PhD thesis, Universität der Bundeswehr München, Fakultät für Luft- und Raumfahrttechnik, 2013.

[13] Stokes, G. G., *On the Effect of the Internal Friction of Fluids on the Motion of Pendulums*. Pitt Press Cambridge, 1851, vol. 9.

[14] Weiss, P.-E., S. Deck, J.-C. Robinet, and P. Sagaut, “On the Dynamics of Axisymmetric Turbulent Separating/Reattaching Flows”, *Physics of Fluids*, vol. 21, no. 7, p. 075 103, 2009.

[16] Wolf, C. C., “The Subsonic Near-Wake of Bluff Bodies”, PhD thesis, Rheinisch-Westfälische Technische Hochschule Aachen, Fakultät für Maschinenwesen, 2013.